A Numerical Investigation of Neel Wall Effects in Amorphous MI Ribbons

Kwaku Eason[1] and Kok-Meng Lee[2], *Fellow, IEEE*

[1]The George W. Woodruff School of Mechanical Engineering, Georgia Institute of Technology, Atlanta, GA 30332-0405 USA
[2]Data Storage Institute, 117608 Singapore

We present new results from modeling the magnetoimpedance (MI) effect, which considers explicitly the experimentally observed stripe domain structure in MI ribbon elements. Specifically, we solve the Maxwell and the Landau–Lifshitz–Gilbert equations formulated in such a way that includes an *a priori* known equilibrium magnetization. The equations are solved numerically for the real and imaginary parts of the magnetic field and magnetization simultaneously using a meshless method formulated in a point collocation scheme. Contrary to other models that have treated domain walls in a lumped parameter approach, we investigate the effects of the experimentally observed 180° Neel walls directly. Additionally, resulting MIR values are computed and compared to published experimental data and the case ignoring domain structure for the amorphous ribbon. It is shown that the presence of the observed domain structure leads to greatly reduced MI voltages, and contributing mechanisms are discussed. Moreover, the results have a broader impact applying to other harmonic magnetic structures with and without 180° Neel walls.

Index Terms—Coupled harmonic micromagnetics, domain wall, magnetoimpedance (MI), meshless methods, MI sensor, micromagnetics, Neel wall.

I. INTRODUCTION

MAGNETOIMPEDANCE (MI) effect sensors represent a class of alternative low-cost highly sensitive magnetic field detectors that have accordingly attracted much attention in recent years. In earlier studies with amorphous Co-based MI sensors, absolute resolution measurements yielding values on the order of 10^{-10} T for steady fields and 10^{-11} T for ac fields were demonstrated [1]. Many MI sensor applications have been suggested in [2]. Interests to extend MI sensor resolution for potential applications (such as detection of human neural signals on the order of 10^{-13} T [3]) have motivated research leading to a better understanding of MI behaviors, and more importantly to accelerate the pace of MI sensor advancements. This paper numerically investigates the effect of a magnetic domain structure in a MI-element subjected to harmonic conditions due to an ac current source.

In early MI sensor research, domain structures have not unanimously been considered as playing an influential role in the MI effect. For example, in [4] it was suggested that domain wall motion is sufficiently dampened for an operating frequency of 1 MHz and therefore, there may be no need to consider domain walls in modeling efforts [4]. Similar remarks have been put forth by others [5]. However, some experimental evidence has also been presented at lower frequencies, for example, in amorphous ribbon elements that suggest domain walls play a substantial role in the MI effect [6]. Additionally, the influence of Neel walls by way of decoupled linear models in relation to the MI effect in ribbons has been discussed in [7] as well as their connection to anisotropy and experimentally determined effective permeabilities [8]. An improved understanding of the role of domain structure also aids in interpretations from extended structures, which have also been investigated (for example, in circular composites and multilayered ribbons [9]). Nevertheless, the existence of a domain structure in MI elements has been confirmed in both amorphous near-zero magnetostriction ribbons and wires [10], [11]. Observations using magneto-optical Kerr effect techniques [11] have shown experimentally that Co-based amorphous ribbons possess the so-called "striped" domain structure with 180° Neel walls. While these experimental observations of domain structures offer valuable insights, it is also desired that the information from these experimental findings can be used in analytical predictions in order to facilitate MI sensor designs.

In [12], we offer a general harmonic formulation (taking into account explicitly the effects of micro-magnetics) for modeling the magnetic fields in structures like the MI element. While relaxing assumptions commonly made in the literature, this coupled nonlinear model provides a means to explicitly solve the Maxwell and the Landau–Lifshitz–Gilbert (M-LLG) equations simultaneously for the real and imaginary parts of the magnetic fields and magnetization. This paper exploits the harmonic coupled nonlinear formulation to accommodate a domain structure, particularly when experimental observations have been made. Specifically, we numerically investigate the effects of the Neel walls on the MI effect.

The remainder of this paper offers the following.

1) We offer a means to accommodate a prior knowledge of an equilibrium domain structure in the coupled set of M-LLG harmonic equations [12] so that the effects of the 180° Neel wall on the inductive voltage across an amorphous ribbon MI element can be analytically investigated.

2) The harmonic formulation (with domain wall considerations for a MI ribbon) is solved numerically using a point-collocation meshless method (PC-MLM) for the magnetic field intensity and magnetization. The PC-MLM algorithm has been validated by comparing solutions to the nonlinear 180° Bloch wall problem that has an exact solution. In ad-
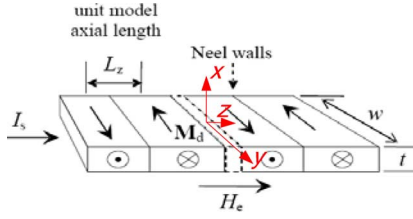
Fig. 1.   Co-based amorphous ribbon domain structure and unit periodic "slice."

dition, we examine factors that significantly influence computational convergence and time with a Galerkin finite element method (FEM) that serves as a basis for comparison.

3) Using the validated PC-MLM, we investigate the effects of the striped domain structure directly on the MI effect by comparing the coupled nonlinear model with and without the domain structure, and against published experimental results. As will be discussed along with the computed results, the presence of the 180° Neel walls has an effect of reducing the inductive voltages in MI ribbon sensors.

With this, the discussion takes the following format: first, the approach for considering the domain structure explicitly is discussed; then the model formulation is outlined followed by a discussion of calculated results. Finally, we conclude with a summary of observations.

II. DOMAIN-WALL EFFECT CONSIDERATIONS

We consider here a MI sensor consisting of an alternating input current source I_s across a magnetic ribbon (thin rectangular amorphous wire) in the presence of relatively weak external magnetic field intensity H_e. The domain structure for the ribbon materials in MI elements at steady (or equilibrium) state has been observed experimentally and is known to possess stripe domains, given by alternating transverse domains separated by Neel walls. The experimentally observed domain structure is schematically illustrated in Fig. 1. The interest here is to investigate the effects of the 180° Neel wall domain structure, both quantitatively and qualitatively (which have been observed experimentally), on the inductive voltage induced across the MI sensor. This is accomplished by solving the coupled set of Maxwell's and Landau-Lifshitz-Gilbert equations (MLLG) for the magnetic field intensity and magnetization

$$\mathbf{H} = H_e\mathbf{e_z} + \mathbf{H_\sim}; \quad \mathbf{M} = \mathbf{M_d}(\mathbf{x}) + \mathbf{M_\sim} \qquad (1a,b)$$

where H_e is the measured dc external field; and $\mathbf{H_\sim}$ is the harmonic component (varying at the input frequency ω) of the magnetic field due to I_s. The magnetization $\mathbf{M}$ has a similar form given by (1b) where $\mathbf{M_d}(\mathbf{x})$ is the (location-dependent) equilibrium magnetization; and $\mathbf{M_\sim}$ is the unknown harmonic deviation from equilibrium.

Equation (1b) provides a means to accommodate a prior knowledge of an equilibrium domain structure, given as $\mathbf{M_d}$, that has been observed experimentally. Generally, the equilibrium magnetization is quantitatively described by [13]

$$\mathbf{M_d}(\mathbf{x}) \times \mathbf{H_T} = 0 \text{ where } \|\mathbf{M_d}(\mathbf{x})\| = M_s \qquad (2a,b)$$

where M_s is the saturation magnetization and $\mathbf{H}_T$ is the total effective field vector defined by

$$\mathbf{H_T} = \mathbf{H} + \mathbf{H_K} + \mathbf{H_X} + \mathbf{H_D} \qquad (3)$$

where $\mathbf{H_K}, \mathbf{H_X}$, and $\mathbf{H_D}$ are the effective fields taking into account anisotropy, exchange, and demagnetization, respectively, and $\mathbf{H}$ is the total external field expressed in (1a). An explicit solution to (2) is nontrivial for MI elements. However, observations in amorphous Co-based ribbons provide qualitatively a domain structure $\mathbf{M_d}$ for the amorphous low-magnetostriction MI element wires. We model $\mathbf{M_d}$ analytically in accordance with the observed periodic nature of the equilibrium structure (Fig. 1) using a general, unit periodic-slice of length L_z. In addition, the following assumptions (with the aid of Fig. 1) are made.

  i) Domain structure is uniform in the y direction.
  ii) x component of the equilibrium magnetization is negligible.
  iii) Neel wall is narrow and its influence vanishes towards the domain center. Thus, in the unit slice sufficiently far from the wall, variations are only in x.

Based on these assumptions, $\mathbf{M_d}$ remains in the y-z plane and its z-component is given by the constraint

$$\bar{\mathrm{M}}_{dz} = \sqrt{1 - \bar{\mathrm{M}}_{dy}^2} \text{ where } \bar{\mathbf{M}}_d = \mathbf{M}_d/M_s.$$

Then, the transverse component assumes the following form:

$$\bar{M}_{dy} = \bar{M}_N(z)\bar{M}_H(H_e) \qquad (4)$$

where $\bar{M}_N(z)$ and $\bar{M}_H(H_e)$ describe the dependence on the Neel wall variation and the external field respectively.

As will be shown, (1)–(4) offer a practical way to intuitively study the effects of the observed domain walls in relation to all the field components predicted using the coupled nonlinear harmonic MLLG equations.

A. Analytic Neel Wall

The Neel walls introduce variations along the z direction. In regions within the unit slice but sufficiently far from the Neel wall centerline

$$\text{at } z = \mp\infty \left.\bar{\mathbf{M}}_d\right|_{z=\mp\infty} = [0 \quad \mp 1 \quad 0]^T. \qquad (5)$$

The boundary conditions (5) suggest that the variation due to the Neel walls can be described by the function (6)

$$\bar{M}_N(z) = \tanh[(p_1 z + z_p)/L_c] \qquad (6)$$

where the parameters, p_1 and z_p, provide a means to scale the wall width and to locate the wall center respectively; and L_c is the characteristic length scale for the domain wall width.

B. H_e Dependence Factor

The dependence of $\mathbf{M_d}$ on H_e, in the absence of time varying fields, can be derived from (2) considering only the dc external

and anisotropy fields (normalized to M_s), as they dominate the effective field in the problem considered

$$\bar{\mathbf{M}}_d \times \left[\bar{H}_e \mathbf{e}_z + \bar{\mathbf{H}}_K \right] = 0. \tag{7}$$

With a known anisotropy direction and negligible x component equilibrium magnetization, (7) leads to an explicit function of the transverse magnetization component $\bar{M}_H$ in terms of the external field H_e

$$\bar{M}_H = 1/\sqrt{1 + (H_e/H_K)^2}. \tag{8}$$

As will be shown with numerical results, the amplitude ratio H_e/H_K has a significant influence on the magnetization and hence the MI induced voltages.

III. COUPLED NONLINEAR HARMONIC FORMULATION

For a MI element subjected to an ac current source and a dc external field, $\mathbf{M}$ and $\mathbf{H}$ are represented as the sum of steady and *ac* components given by

$$\mathbf{H} = \mathbf{H}_e + \mathbf{H}_\sim e^{-j\omega t + \phi} = \mathbf{H}_e + \mathbf{H}_R + j\mathbf{H}_I \tag{9a}$$
$$\mathbf{M} = \mathbf{M}_d + \mathbf{M}_\sim e^{-j\omega t + \phi_M} = \mathbf{M}_d + \mathbf{M}_R + j\mathbf{M}_I. \tag{9b}$$

The subscripts "R" and "I" denote the real and imaginary parts. The Neel wall domain structure in (4) can now be accounted for directly in the coupled nonlinear harmonic formulation based on the Maxwell's and the Landau–Lifshitz–Gilbert (LLG) equations.

The coupled set of nonlinear harmonic PDEs is given by (10)–(12). Specifically, (10a,b) are equations for the magnetic field intensity within the ribbon MI element

$$\nabla \times \nabla \times \mathbf{H}_R + \sigma\omega(\mu_0\mathbf{H}_I + \mathbf{M}_I) = 0 \tag{10a}$$
$$\nabla \times \nabla \times \mathbf{H}_I - \sigma\omega(\mu_0\mathbf{H}_R + \mathbf{M}_R) = 0 \tag{10b}$$

where σ is the bulk electrical conductivity and μ_o is the permeability of free space. Similarly, in harmonic vector form the modified form of the LLG equation governing the magnetization "motion" are given by (11a, b), [12]

$$\frac{\omega}{\gamma}([\Gamma_I]\mathbf{M}_R + [\Gamma_R]\mathbf{M}_I) = \mathbf{M}_I \times \mathbf{H}_{TI} - (\mathbf{M}_d + \mathbf{M}_R) \times \mathbf{H}_{TR} \tag{11a}$$
$$\frac{\omega}{\gamma}(\Gamma_R\mathbf{M}_R - \Gamma_I\mathbf{M}_I) = \mathbf{M}_I \times \mathbf{H}_{TR} + (\mathbf{M}_d + \mathbf{M}_R) \times \mathbf{H}_{TI} \tag{11b}$$

where γ is the gyromagnetic ratio. In (11a,b), $[\Gamma_R]$ and $[\Gamma_I]$ are the real and imaginary components of

$$[\mathbf{\Gamma}] = [\mathbf{I}] - (\alpha/M_s)\text{Skew}(\mathbf{M}). \tag{11c}$$

Similarly, $\mathbf{H}_{TR}$ and $\mathbf{H}_{TI}$ are the real and imaginary parts of

$$\mathbf{H}_T = \mathbf{H} + (2K/M_s^2)(\mathbf{M} \cdot \mathbf{e}_K)\mathbf{e}_K + A\nabla^2\mathbf{M} - \nabla\varphi_D \tag{11d}$$

where $\mathbf{e}_K$ is the unit vector in the direction of the material preferred anisotropy; K is the first anisotropy constant; and A is the exchange stiffness. The last term in (11d) accounts for the effects of demagnetization described by

$$\mu_0\nabla^2\varphi_{DR} = \nabla \cdot \mathbf{M}_R; \text{and } \mu_0\nabla^2\varphi_{DI} = \nabla \cdot \mathbf{M}_I. \tag{12a,b}$$

A. Boundary Conditions (BCs)

The computational model considers variations in the x-z plane with a periodic domain structure. The BCs for the x component are given by (13) and (14), where (14g) assumes the free spinning condition at the surface

$$x = 0 \quad \partial\mathbf{H}/\partial x = \partial\mathbf{M}/\partial x = \varphi_D = 0 \tag{13}$$
$$x = t/2 \quad \mu_0(H_{xR} + jH_{xI}) = -(M_{xR} + jM_{xI}) \tag{14a,b}$$
$$H_{Ry} = I_s/2w; \quad H_{Iy} = 0 \tag{14c,d}$$
$$H_{zR} = H_{zI} = 0 \tag{14e,f}$$
$$\partial\mathbf{M}/\partial x = 0 \tag{14g}$$
$$\mu_0\partial(\varphi_{DR} + j\varphi_{DI})/\partial x = M_{xR} + jM_{xI}. \tag{14h}$$

Note that the field intensity at the interface $(x = t/2)$ can be obtained by integrating Amperes law over the cross-sectional area because of the current source, which leads to (14).

The observed periodic nature with assumption iii) on relatively narrow walls suggests that the solutions at the z boundaries approach the solution to the 1-D model that has a uniform domain structure, keeping all other parameters the same. Thus, a high density solution of the 1-D problem is enforced at the axial ends of the slice

$$z = \mp\infty : \mathbf{f}(x, z; H_e, \mathbf{M}_d)|_{z=\mp\infty}$$
$$= \mathbf{f}(x; H_e, \mathbf{M}_d)|_{z=\mp\infty}. \tag{15}$$

It is noted that from (15), aside from a collapsed model only varying in x, at $z = -\infty$ (left end), $\mathbf{M}_d = \begin{bmatrix} 0 & -1 & 0 \end{bmatrix}^T$ and the oppositely oriented equilibrium state exists at $z = +\infty$. Thus, the only difference in the 1-D model at each slice boundary is the local equilibrium magnetization orientation. Due to the consistency of the 1-D and 2-D equations, and the boundary conditions, the formulation discussed above avoids the need for special considerations at the corners of the computation domain, which has been discussed in [14].

B. Calculations of MI Ratio (MIR)

Once the magnetization $\mathbf{M}$ and field intensity $\mathbf{H}$ are known, the MI inductive voltage can be calculated by

$$V_L = -\frac{d\Phi}{dt} \text{ where } \Phi = \int_S (\mu_0 \mathbf{H} + \mathbf{M}) \cdot d\mathbf{s} \qquad (16)$$

where S is the flux crossing area in the x-z plane of the ribbon. Adding the ohmic voltage for the total MI voltage, V, the MI ratio (MIR) in percent is then found from

$$\mathrm{MIR}(\%) = 100[V(H_e) - V(0)]/V(0). \qquad (17)$$

IV. NUMERICAL CONSIDERATIONS

The coupled set of harmonic equations (with domain wall considerations for a MI ribbon) is solved numerically using a point collocation meshless method (PC-MLM). Motivated by the interest to perform all simulations on a desktop PC we base the model on the observed periodic Neel wall enabling a reduction of the computational domain to a general unit slice of length, L_z (see Fig. 1). This eliminates the need to model all the magnetic domains (which are many) along the entire length of the ribbon, and hence greatly reduces computational demands. In addition, we examine factors influencing the convergence and computational time of the PC-MLM. In the following discussions, the computations were based on a desktop Pentium IV PC (3.5 GHz, 3.5 GB-RAM),

A. PC-MLM Validation and Computational Effectiveness

The PC-MLM numerical algorithm is validated by comparing solutions to the nonlinear 180° Bloch wall problem that has an exact solution given in Appendix A, where x is the independent variable. Here, the angle distribution $\phi(x)$ that minimizes the system energy is computed. In addition, we evaluate the following two shape functions (Appendix B and C) in PC-MLM for their rates of computational convergence

- Hp cloud shape functions (HP-PC) [15], [16];
- Radial basis functions (RBF-PC) [17].

For this, a Galerkin finite-element method is employed to serve as a basis for comparison. The following terms are used in evaluating the convergence of the algorithms.

- *Energy norm*, $\|E\|_2 \doteq \sqrt{\int_\Omega (\phi - \phi_{\mathrm{exact}})^2 dx}$.
- *Incremental approximate error*, $e_a = |\phi_{i+1} - \phi_i|/|\phi_{i+1}|$.
- *Computation time* T normalized to the longest time $T_{\max}$ of all computation cases being compared.

The exact solution and minimized energy profile across the wall are given in Fig. 2, where x is normalized to the characteristic length $L_c = \sqrt{A/K}$ for the wall width t_w (see Fig. 9). With a sufficient number of nodes and iterations, all three numerical algorithms (HP-PC, RBF-PC, and finite-element method) converge to the exact solution. The comparisons are presented in Fig. 3, where $T_{\max} = 89$ min corresponding to the finite-element method computation with 115 nodes (or 57 of second-order elements). From results of the 180° Bloch wall model,

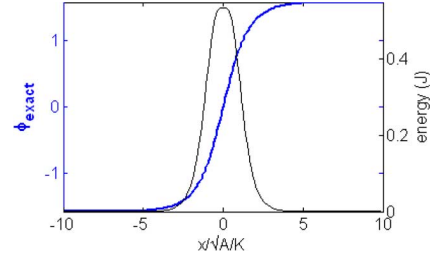Fig. 2. Exact solution to the 180° Bloch wall problem (Appendix A).

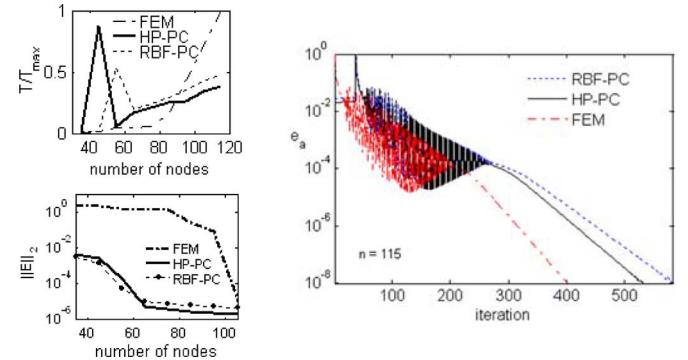
Fig. 3. Convergence of 180° Bloch wall solutions.

the HP-PC formulation is chosen based on the following observations.

- The PC-MLM converges to an acceptable error faster than finite-element method with a lower computation time. This observation is similar to that published in [14] where a (noninterpolating) reproducing kernel particle shape function was used in a PC-MLM for solving linear magnetic problems.
- The comparisons show that the HP-PC converges slightly faster than the RBF-PC. This observation is likely due to the compactness of the Hp-Cloud shape functions used here leading to a more diagonally dominant Jacobian matrix, where RBF shape functions using thin-plate splines are generally not compact (Appendix C).

B. Nonlinear Solver Based on Quasi-Newton Method

Newton's method has been a principal tool for solving a system of nonlinear equations, which is generally quadratic in convergence. However, it is required to compute, at each iteration, a Jacobian matrix and inverse. For the 2-D problem considered, each node has 14 degrees of freedom (real and imaginary components of vectors $\mathbf{H}_\sim, \mathbf{M}_\sim$, and scalar φ_D). The total number of functional evaluations and arithmetic operations for each of the iterations is approximately given by

$$n_{\mathrm{feval}} \approx 28n_c^2 + 14\vartheta\left(n_c^3\right) \qquad (18)$$

where n_c is the number of computational nodes; and the term $\vartheta(n_c^3)$, which denotes on the order of n_c^3, often dominates.

To reduce the computation cost for the 2-D MI element model, a quasi-Newton method known as Broyden's method

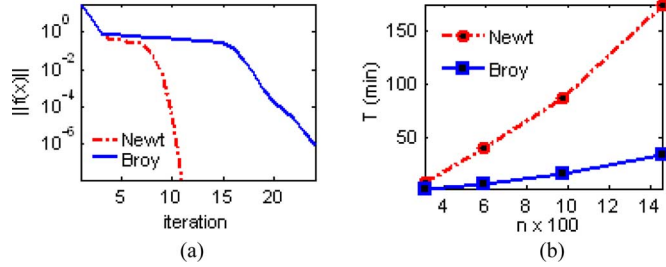| M_s (T)	H_K (A/m)	A (J/m)	α	σ $(m\Omega\text{-cm})^{-1}$	p_1	z_p	L_z (μm)
1.39	478	10^{-11}	0.01	7.6923	1	0	100

Fig. 4. Newton and Broyden comparisons (2-D ribbon model; $\mathrm{tol} = 10^{-6}$). (a) convergence of f(x) and (b) solver computation time, T.

Fig. 5. Nonlinear and linear 1-D solutions to H_y (=7 μ T, and $H_e = 0$). (a) Real component of H_y and (b) imaginary component of H_y.

[18] with an optimized line search [19] has been deployed here. The Broyden's method replaces the Jacobian matrix in Newton's method with an approximate "updated" matrix (see Appendix D). While the quadratic convergence of Newton's solver is lost to superlinear convergence, the quasi-Newton method requires $\vartheta(n_c^2)$ and as will be shown in the 2-D solutions, the Broyden update scheme offers a more than acceptable trade-off for the time savings.

Case Study Example: To illustrate this trade off, we compare the quasi-Newton method with a Broyden update scheme (given in Appendix D) against the Newton's solver for the 2-D MI ribbon element model. Listed in Table I, the values of the parameters used in the simulation have been based on [6] for a 40 μm thick amorphous ribbon element subjected to an *ac* current source ($I_s = 10$ mA, $f = 120$ kHz), so that comparisons can be made against published experimental data. The parameters, p_1 and z_p, from the analytic domain structure (4) are also included in Table I.

In Table I, M_s was computed using the volume compositional average based on published values for Co and Fe [20] for the experimental material, $Co_{70.4}Fe_{4.6}Si_{12.5}B_{10}$. The preferred anisotropy direction is assumed uniformly transverse throughout the ribbon ($e_K = \begin{bmatrix} 0 & 1 & 0 \end{bmatrix}^T$). The gyro-magnetic ratio is given (in SI units) by $\gamma = \mu_0 g q_e / 2m_e$ [21], where the g-factor $g \approx 2$, q_e is the electron charge; and m_e is the electron mass. The characteristic length scale L_c used here is given by

$$L_c = \sqrt{A/K} \text{ where } K = M_s H_K / 2. \quad (19)$$

Using Table I, $K = 332.5$ J/m^3 and $L_c = 0.1734$ μm.

Fig. 4 illustrates the tradeoff between convergence and computation time when using a quasi-Newton method with a Broyden update scheme in the 2-D ribbon solution. Both methods (direct Jacobian computation and *Broyden's* update) use an optimized line search. The convergence and computation time are compared for $n_c = 5 \times 5, 7 \times 7, 9 \times 9$ and 11×11 nodes, which corresponds to 350, 686, 1134, and 1694
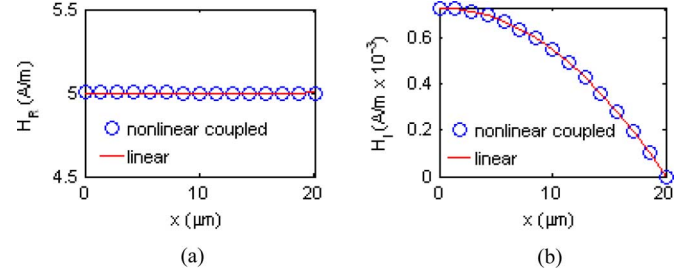
unknowns (since each node has 14 degrees of freedom; real and imaginary components of $H_\sim$, $M_\sim$ and φ_D).

As shown in Fig. 4, the Broyden's update scheme takes significantly more iterations to converge (Fig. 4(a)). However, when the degrees of freedom become large, the reduction of functional evaluations from $\vartheta(n_c^3)$ to $\vartheta(n_c^2)$ saves considerable computation time as demonstrated in Fig. 4(b) where $n(= 14n_c$ is the total number of unknowns. Thus, the quasi-Newton method with the Broyden's update scheme is deployed in the remaining problems considered.

V. RESULTS AND DISCUSSION

Three sets of solutions have been numerically obtained for the 2-D MI ribbon element (Case Study Example in Section IV with values listed in Table I); linear 1-D model $(M_s = H_e = 0)$, 1-D nonlinear model, and 2-D coupled nonlinear model.

A. Linear Model $(M_s = H_e = 0)$

For the case of vanishing M_s, the 1-D model converges to the exact solution [22] for linear H_y in a ribbon

$$H_y = C_b \cosh(kx) \text{ where } k^2 = -j\omega\mu_0\sigma. \quad (20)$$

Using the boundary condition specified in (14c, d), the constant C_b is determined to be 5. The *first* set of solutions for a very small M_s in the absence of external field ($H_e = 0$) is given in Fig. 5, where the exact solution for linear H_y (20) serves as a basis for validating the 1-D nonlinear model.

B. 1-D Boundary Model at $z = \mp\infty$

The coupled nonlinear model utilizes a 1-D solution as a boundary condition (15). For this, the 1-D coupled nonlinear model (75 nodes) is solved at both ends of the slice ($z = \mp\infty$) where the respective equilibrium domain structures are given by (5). Unlike (20), this 1-D model (in x) accounts directly for both H_e and the alternating 180° equilibrium magnetization while keeping the transverse anisotropy uniform throughout the structure.

As will be discussed, the maximum MI voltage occurs when $H_e/H_K \approx 1$ for transverse anisotropy in MI ribbons. Hence, the *second* solution set (Fig. 6) simulates (both magnitudes and phases of) H_y and M_y in the MI ribbon for $H_e/H_K = 0.99$.
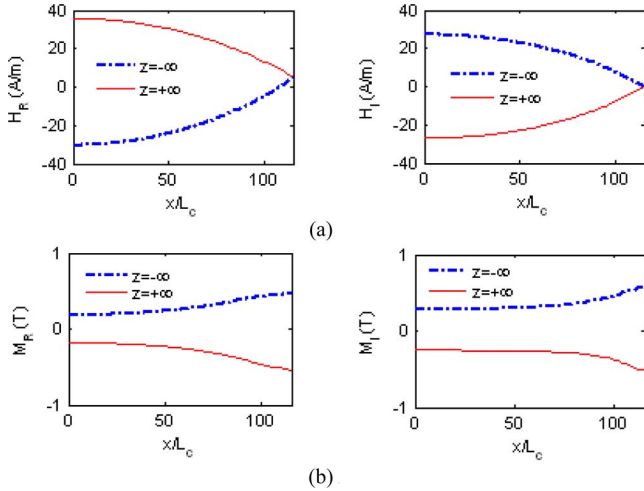
Fig. 6. 1-D Solutions of MI ribbon element ($z = \mp\infty$). (a) H_y solutions and (b) M_y solutions.

C. 2-D Coupled Nonlinear Harmonic Solutions (With Neel Walls)

With the 1-D boundary solution, the *third* solution set simulates the effect of $\bar{M}_N(z)$ and $\bar{M}_H(z)$ using the 2-D coupled nonlinear harmonic model which explicitly accounts for the domain wall effect (4). The 2-D solutions were solved using 17×17 nodes for the H_y and M_y components, and are presented in Figs. 7(a) and (b).

To illustrate the effect of a small H_e on the MI ratio, two additional data at $0.6 H_K$ and $0.1 H_K$ were computed. The amplitude surfaces of the transverse M_R and M_I are shown in Figs. 7(b), (c), and (d) for all three values of external fields ($H_e/H_K = 0.99, 0.6$ and 0.1, respectively).

The MI ratios are compared in Table II against published experimental data [6] that serves as a basis for comparison, and the 1-D coupled nonlinear solution ignoring domain structure.

D. Observations and Discussions

The following observations are made from the results (Figs. 5–7 and Table II).

a) Table II shows that the 2-D coupled nonlinear model (Section III) with the domain structure (4) leads to predictions much closer to experimental data [6] than the 1-D solution ignoring domain structure. These results suggest that the Neel walls play an influential role in reducing the MIR in MI ribbons. The discrepancies between experimental data and 2-D numerical results in Table II may partly be due to a) the simplified treatment of the H_e variation and b) the sizing differences between the domains along the axis, where equal sized domains have been assumed.

b) As shown in Figs. 5 and 6(a), except at the boundary condition (at $x = t/2$) the linear decoupled model (20) departs from the coupled nonlinear 1-D boundary model (15) that provides a means to include different $\mathbf{M}_d$ equilibrium states. The influence of $M_d(z = \mp\infty)$ can be seen in the magnitude and phase of the H_y solutions. As graphed in Fig. 8, the alternating orientation of $M_d(z = \mp\infty)$ along the ribbon contributes to
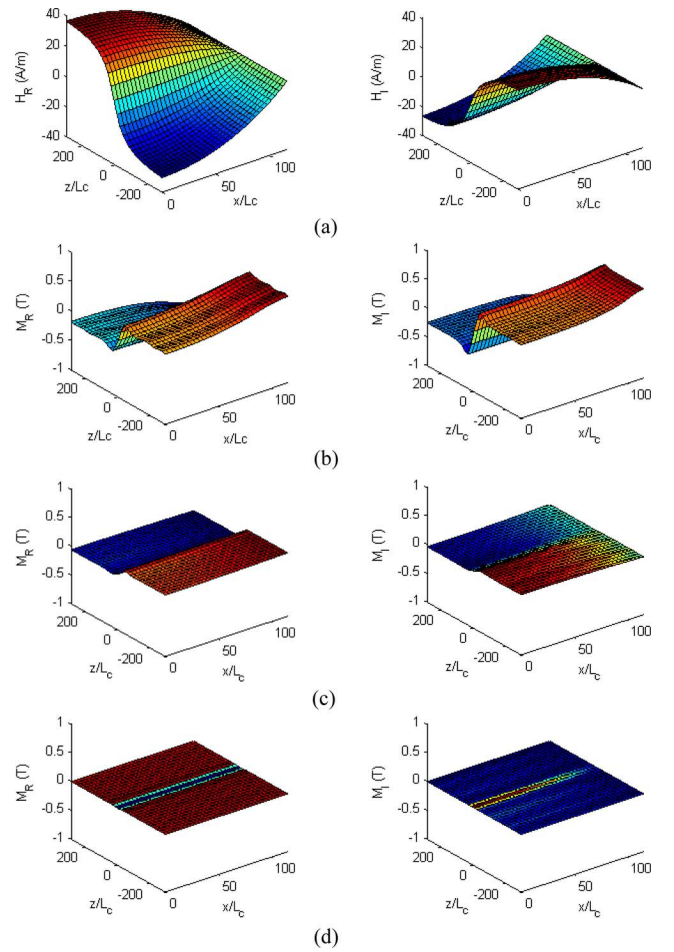

Fig. 7. 2-D solutions of MI ribbon element. (a) H_y for $H_e/H_K = 0.99$, (b) M_y for $H_e/H_K = 0.99$, (c) M_y for $H_e/H_K = 0.6$, and (d) M_y for $H_e/H_K = 0.1$.

TABLE II
MIR COMPARISONS

H_e/H_K	Experiment [6]	2D model with domain structure	1D model ignoring domain structure
0.99	45 %	117 %	1941 %
0.60	10 %	30 %	406 %
0.10	1 %	1.7 %	1 %

- 180° phase difference between $H_y(z \to -\infty)$ and $H_y(z \to +\infty)$;
- slight magnitude difference between $|H_y(z \to -\infty)|$ and $|H_y(z \to +\infty)|$.

The asymmetry in magnitude may be explained as follows. As a result of the alternating orientation of the domain structure, the induced currents (described by Amperes law) have equal and opposite signs on the right and left sides of the unit slice; this leads to equal and opposite gradients of H_y along x within the ribbon. Consequently the presence of the (real) current I_s "shifts" the real H_y component distribution [Fig. 6(a)] away from 0 at the surface on both sides creating the asymmetry indicated in Fig. 8(a). Similar (but nonlinear) asymmetry can be seen in the M_y magnitude in Fig. 8(b).

In addition to the influence of $\mathbf{M}_d$ on the edges of the slice (discussed above), Fig. 7 shows that the Neel wall apparently provides ripe conditions for an analogous transition between the harmonic components deep in the domain interior, represented as the edges of the slice. The effect of the Neel wall that can be seen in all components shows that the solutions, in general, depend on the presence of a domain structure.

c) Fig. 7(a) shows that the H_y distributions develop in both x and z as the amplitude ratio H_e/H_K approaches 1. Reducing or increasing H_e/H_K relative to unity display similar behaviors. In a weak field below the anisotropy field $(0 < H_e/H_K < 1)$, the $\mathbf{M}_\sim$ amplitudes rapidly decrease as H_e/H_K goes from 1 to 0 as shown in Figs. 7(b) to (d). In fact, the M_y amplitude when $H_e/H_K = 0.6$ is an order of magnitude smaller than that when $H_e/H_K = 0.99$, and nearly vanishes when $H_e/H_K = 0.1$. Physically, the decrease in M_y amplitudes with H_e in MI ribbons can be explained by broadly dividing the amplitude ratio H_e/H_K into three regions; $H_e/H_K \ll 1, \approx 1$, and $\gg 1$.

- When $H_e/H_K \ll 1$, the magnetization is firmly oriented by the transverse anisotropy field, H_K, (as it dominates at 478 A/m) in the very weak field region. As $H_y \sim 40$ A/m, the magnetization is less sensitive to H_y under these transversely dominant conditions.
- When H_e (along z) approaches H_K in amplitude, this creates conditions that reorient $\mathbf{M}_d$ more along the z direction increasing the sensitivity to the transverse alternating field up to a cutoff point near H_K.
- Beyond the anisotropy field, the magnetization aligns in a more stable configuration along z, and as $H_e/H_K \gg 1$, an analogous stable configuration develops along z.

d) The presence of an axial z component relative to the transverse component $(H_e/H_K \approx 1)$ may contribute to the observed larger amplitude oscillations for the MI configuration generating larger voltages. This is consistent with observations in [12] where relatively large MI induced voltages are seen in the circular wire with completely axially oriented domains and much smaller anisotropy. It is also interesting to note that the highest sensitivities (between ribbon and circular elements) reported in MI sensors have been in circular wires which have either no Neel walls (composites) or smaller volumes occupied by Neel walls, while the rest is aligned axially in the circular amorphous wires [10]. These observations may be related.

e) As shown in Fig. 7, a large portion of the ribbon largely favors the boundary solutions. The Neel wall region, though accounts for a relatively small areal region where variation along z occurs, leads to magnetic flux cancellation over the ribbon. Thus, the domain structure with Neel walls has an effect to reduce the inductive voltage (over the length of the ribbon along the z axis).

VI. CONCLUSION

We have presented results modeling numerically the experimentally observed stripe domain structure in MI ribbon elements. This has been enabled by use of a MLM point collocation
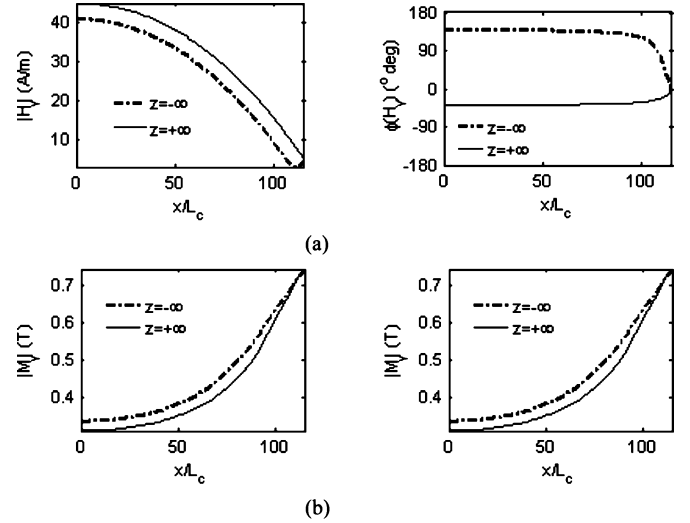

Fig. 8. Effects of $M_d(z = \mp\infty)$ based on 1-D boundary model $(z = \mp\infty)$. (a) Magnitude and phase of $H_y(z = \mp\infty)$ and (b) magnitude and phase of $M_y(z = \mp\infty)$.

formulation along with a selective Broyden nonlinear scheme to solve the proposed model. The algorithm has been validated by comparing solutions to the nonlinear 180° Bloch wall problem that has an exact solution as well as published experimental data.

The effects of the Neel walls and the amplitude ratio H_e/H_k on the magnetization and on the MIR of a 2-D MI ribbon have been numerically investigated. Results from the 2-D coupled nonlinear model with domain structure not only show quantitative effects consistent with prior works, but also indicates a radical departure, qualitatively, from decoupled classical models in that influence of the domain structure itself has been shown to influence both the magnetic field intensity, as well as the magnetization amplitudes. This distinction leads to a peculiar flux reduction mechanism resulting from oppositely oriented oscillations in the ribbon due to the Neel walls that effectively reduces the voltage drop across the axis of the ribbon. This leads to greatly reduced MIR values, much more consistent with published experimental data.

We also note that these observations have been made in the relatively small external field region $0 < H_e < H_K$, where the domain structure is more "in tact" before saturation. Otherwise, a linearized model offers a good approximation of behavior. Therefore, the role of the stripe domains that has been summarized provide a mechanistic picture of the role of Neel walls in MI elements, which is not possible to obtain readily using a decouple model.

APPENDIX A
180° BLOCH WALL MODEL

Fig. 9 illustrates an 180° Bloch wall, where the magnetization remains in the plane normal to x as its orientation changes from $-\pi/2$ to $\pi/2$. The total magnetization energy of an 180° Bloch wall is given by the integral of the exchange and anisotropy energies (per unity area) [22]

$$E_m = \int_{-\infty}^{\infty} [A(d\phi/dx)^2 + (K/4)\sin^2(2\phi)]dx \qquad (A1)$$
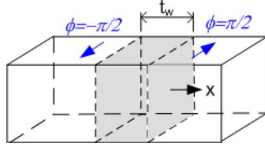
Fig. 9. Classical 180° Bloch wall.

where ϕ is the angle of the equilibrium magnetization relative to the anisotropy direction.

The equilibrium magnetization angle ϕ can be found by minimizing the energy using the variational form of (A1) or $\delta E_m = 0$, which leads to the following Euler-Lagrange equation:

$$4(d^2\phi/dX^2) + \sin(4\phi) = 0 \text{ where } X = x/L_c \qquad (A2)$$

and $L_c = \sqrt{A/K}$ is the characteristic length for the domain wall width t_w. For the uniform 180° domains with the two Dirichlet boundary conditions, $\phi(\pm\infty) = \pm\pi/2$, the closed form solution is given by

$$\phi = 2\tan^{-1}(e^X) - \pi/2 \qquad (A3)$$

APPENDIX B
SHAPE FUNCTIONS USED IN HP-CLOUD FORMULATED PC-MLM

In MLMs, the approximated solution u at point $\mathbf{x}(x, y)$ can be written as

$$u(\mathbf{x}) \cong \sum_{k=1}^{p} \varphi_k a_k = \varphi_v \mathrm{A} \qquad (B1)$$

where φ_k is the basis function; a_k is the nodal control value at the kth node; and $\mathbf{A}$ is a vector of basis function coefficients. For a second-order polynomial-reproducible 2-D formulation, the $p = 6$ basis functions $\{\varphi\}$ used in the Hp-Cloud shape functions [15], [16] are given by

$$\{\varphi\} = \left\{ 1, \frac{x_k - x}{\rho_x}, \frac{y_k - y}{\rho_y}, \left(\frac{x_k - x}{\rho_x}\right)^2, \right.$$
$$\left. \left(\frac{x_k - x}{\rho_x}\right)\left(\frac{y_k - y}{\rho_y}\right), \left(\frac{y_k - y}{\rho_y}\right)^2 \right\} \qquad (B2)$$

where (x_k, y_k) represents a point from the local support domain which is a subset of the computational domain. Formulated using a moving least square

$$\mathbf{A} = \mathbf{M}^{-1}\mathbf{T}\mathbf{U} \qquad (B3)$$

the elements of $\mathbf{M}(\in \mathbf{R}^{p \times p})$ and $\mathbf{T}(\in \mathbf{R}^{p \times n})$ matrixes are given by (B4)

$$T_{ik} = w(\mathrm{x}_k - \mathrm{x}; \rho) \cdot \varphi_i(\mathrm{x}_k - \mathrm{x}; \rho) \quad \text{and}$$
$$M_{ij} = \sum_{k=1}^{n} \varphi_i w(\mathrm{x}_k - \mathrm{x}; \rho)\varphi_j \qquad (B4)$$

where the weighting function $w(\mathbf{x})$ in (B4) is given by

$$w(\mathbf{x}) = w_x(\mathbf{x})w_y(\mathbf{x})$$
$$= [1 - (\|x - x_j\|/\delta_x)^{-8}][1 - (\|y - y_j\|/\delta_y)^{-8}] \quad (B5)$$

where $\mathbf{U}$ is the vector of unknowns, $u(\mathbf{x})$ at each support node, (x_k, y_k).

APPENDIX C
RADIAL BASIS FUNCTION USED IN PC-MLM

For the radial basis functions deployed in a formulation that results in a partition of unity (POU), the approximation takes the form [17]

$$u^p(\mathbf{x}) = \sum_{j=1}^{n} B_j(\mathbf{x})a_j + \sum_{j=1}^{p} M_j(\mathbf{x})b_j = \bar{\mathrm{B}} \cdot \bar{\mathrm{A}}. \qquad (C1)$$

A linear system of equations is built by evaluating (C1) at all n local support nodes at all p polynomial basis functions. This process leads to the moment matrix defined by

$$\bar{\mathrm{A}} = \mathrm{M}_{\mathrm{RBF}}^{-1} \begin{bmatrix} \mathrm{U} \\ 0 \end{bmatrix} \text{ where } \mathrm{M}_{\mathrm{RBF}} = \begin{bmatrix} \mathrm{B_r} & \mathrm{M}_p \\ \mathrm{M}_p^T & 0 \end{bmatrix}. \qquad (C2)$$

In (C2), the basis functions in the moment matrix are given by

$$\begin{bmatrix} \mathrm{U} \\ 0 \end{bmatrix} = \begin{bmatrix} \mathrm{B_r} & \mathrm{M}_p \\ \mathrm{M}_p^T & 0 \end{bmatrix} \begin{bmatrix} \mathrm{A} \\ \mathrm{B} \end{bmatrix} = \mathrm{M}_{\mathrm{RBF}}\bar{\mathrm{A}}. \qquad (C3)$$

This leads to the solution for the basis function coefficients, given by

$$M_{ij} = B_j(\mathrm{x_i}) \text{ and } M_{p,ik} = P_k(\mathrm{x_i}) \qquad (C4)$$

where B_j is the radial basis function, where thin plat splines are used [17], and P_k is the monomial basis function similar to that given in (B2).

APPENDIX D
QUASI-NEWTON METHOD USING BROYDEN UPDATE RULE

The quasi-Newton method has an update rule of the form

$$\mathbf{x}^{k+1} = \mathbf{x}^k - \hat{\alpha}\tilde{\mathbf{J}}_k^{-1}\mathbf{f}(\mathbf{x}^k) \qquad (D1)$$

where $\tilde{\mathbf{J}}_k$ is computed using a Broyden update rule; and $\hat{\alpha}$ is found from a line search by solving the optimization problem defined by

$$\frac{\partial}{\partial\alpha}\|\mathbf{f}(\alpha)\|^2 = 0. \qquad (D2)$$

In (D1), $\tilde{\mathbf{J}}_k^{-1}$ can be computed from $\tilde{\mathbf{J}}_{k-1}^{-1}$ using the Sherman-Morrison formula [18], eliminating the need for a matrix inver-

sion with each iteration. The resulting inverted update matrix is then given by

$$\tilde{\mathbf{J}}_k^{-1} = \tilde{\mathbf{J}}_{k-1}^{-1} + \frac{\left(\boldsymbol{\delta} - \tilde{\mathbf{J}}_{k-1}^{-1}\boldsymbol{\gamma}\right)}{\boldsymbol{\delta}^{\mathrm{T}}\tilde{\mathbf{J}}_{k-1}^{-1}\boldsymbol{\gamma}}\boldsymbol{\delta}^{\mathrm{T}}\tilde{\mathbf{J}}_{k-1}^{-1} \tag{D3}$$

where

$$\boldsymbol{\delta} = \mathbf{x}_{k-1} - \mathbf{x}_{k-2} \tag{D4}$$

and

$$\boldsymbol{\gamma} = \mathbf{f}(\mathbf{x}_{k-1}) - \mathbf{f}(\mathbf{x}_{k-2}). \tag{D5}$$

REFERENCES

[1] K. Mohri, T. Uchiyama, and L. V. Panina, "Recent advances of micro magnetic sensors and sensing application," *Sens. Actuators A*, vol. 59, pp. 1–8, 1997.

[2] K. Mohri, T. Uchiyama, L. P. Shen, C. M. Cai, and L. V. Panina, "Sensitive micro magnetic sensor family utilizing magneto-impedance (MI) and stress-impedance (SI) effects for intelligent measurements and controls," *Sens. Actuators A., Phys.*, vol. A91, pp. 85–90, 2001.

[3] O. V. Lounasmaa and H. Seppa, "SQUIDs in neuro- and cardiomagnetism," *J. Low Temp. Phys.*, vol. 135, pp. 295–335, 2004.

[4] D. Atkinson and P. T. Squire, "Experimental and phenomenological investigation of the effect of stress on magneto-impedance in amorphous alloys," *IEEE Trans. Magn.*, vol. 33, no. 5, pp. 3364–3366, Sep. 1997.

[5] N. A. Usov, A. S. Antonov, and A. N. Lagar'kov, "Theory of giant magneto-impedance effect in amorphous wires with different types of magnetic anisotropy," *J. Magn. Magn. Mater.*, vol. 185, pp. 159–173, 1998.

[6] F. L. A. Machado, C. S. Martins, and S. M. Rezende, "Giant magnetoimpedance in the ferromagnetic alloy $Co_{75-x}Fe_xSi_{15}B_{10}$," *Phys. Rev. B*, vol. 51, pp. 3926–3929, 1995.

[7] L. V. Panina, K. Mohri, T. Uchiyama, M. Noda, and K. Bushida, "Giant magneto-impedance in Co-rich amorphous wires and films," *IEEE Trans. Magn.*, vol. 31, no. 2, pp. 1249–1260, Mar. 1995.

[8] R. G. Ho, Y. Seong-Cho, K. C. Gi, and H. K. Lachowicz, "Change of permeability and GMI in amorphous $Co_{71}Fe_1Mo_1Mn_4Si_{14}B_9$ alloy before and after heat treatment," *IEEE Trans. Magn.*, vol. 35, no. 5, pp. 3391–3393, Sep. 1999.

[9] S. Iida, D. Suzuki, S. Kambe, and O. Ishii, "Enhancement in the magneto-impedance (MI) effect of multi-ribbon," *IEEE Trans. Magn.*, vol. 36, no. 5, pp. 3661–3663, Sep. 2000.

[10] J. Yamasaki, F. B. Humphrey, K. Mohri, H. Kawamura, H. Takamure, and R. Malmhall, "Large Barkhausen discontinuities in Co-based amorphous wires with negative magnetostriction," *J. Appl. Phys.*, vol. 63, pp. 3949–3951, 1988.

[11] A. D. Santos, L. G. C. Melo, C. S. Martins, F. P. Missell, Y. Souche, F. L. A. Machado, and S. M. Rezende, "Domains and giant magnetoimpedance in amorphous ribbons by magneto-optical Kerr effect," *J. Appl. Phys.*, vol. 79, pp. 6546–6548, 1996.

[12] K. Eason and K. M. Lee, "Effects of nonlinear micromagnetic coupling on a weak-field magneto-impedance sensor," *IEEE Trans. Magn.*, vol. 44, no. 8, pp. 2042–2048, Aug. 2008.

[13] W. F. Brown, *Micromagnetics*. New York: Wiley, 1963.

[14] K.-M. Lee, Q. Li, and H. Sun, "Effects of numerical formulation on magnetic field computation using meshless methods," *IEEE Trans. Magn.*, vol. 42, no. 9, pp. 2164–2171, Sep. 2006.

[15] C. A. M. Duarte and J. T. Oden, "HP Clouds—A meshless method to solve boundary-value problems," Univ. Texas at Austin, Tech. Rep. 95-05, 1995.

[16] C. A. Duarte and J. T. Oden, "H-p clouds—An h-p meshless method," *Numer. Methods Partial Differential Equations*, vol. 12, pp. 673–705, 1996.

[17] X. Liu, G. R. Liu, K. Tai, and K. Y. Lam, "Radial point interpolation collocation method (RPICM) for the solution of nonlinear Poisson problems," *Comput. Mech.*, vol. 36, pp. 298–306, 2005.

[18] R. L. Burden and J. D. Faires, *Numerical Analysis*. New York: PWS, 1993.

[19] K. J. Beers, *Numerical Methods for Chemical Engineering: Applications in MATLAB*. Cambridge, U.K.: Cambridge Univ. Press, 2007.

[20] J. S. Stohr and H. C. Siegmann, *Magnetism: From Fundamentals to Nanoscale Dynamics*. New York: Springer, 2006.

[21] *Spin Dynamics in Confined Magnetic Structures II*, ser. Topics in Applied Physics, B. Hillebrands and K. Ounadjela, Eds. New York: Springer, 2003, vol. 87.

[22] C. Kittel, "Theory of the dispersion of magnetic permeability in ferromagnetic materials at microwave frequencies," *Phys. Rev.*, vol. 70, pp. 281–290, 1946.

[23] C. Kittel, "Physical theory of ferromagnetic domains," *Rev. Modern Phys.*, vol. 21, pp. 541–583, 1949.